Journal of Geophysical Research: Solid Earth

RESEARCH ARTICLE
10.1029/2018JB016421

Intraplate Strike-Slip Faulting, Stress Accumulation, and Shear Localization of a Crust-Upper Mantle System With Nonlinear Viscoelastic Material

Xuelei Zhang[1] **and Takeshi Sagiya**[1,2]

[1]Graduate School of Environmental Studies, Nagoya University, Nagoya, Japan, [2]Disaster Mitigation Research Center, Nagoya University, Nagoya, Japan

Key Points:
- We develop a self-consistent earthquake cycle model for simulating the evolution of a strike-slip fault with nonlinear Maxwell rheology
- The fault behaviors change with time as the stress accumulates in the upper crust and the deformation concentrates in the lower crust
- Time to develop a lower crustal shear zone with large shear strain is much longer than the time for the localization of deformation

Correspondence to:
X. Zhang,
zhang@seis.nagoya-u.ac.jp

Citation:
Zhang, X., & Sagiya, T. (2018). Intraplate strike-slip faulting, stress accumulation, and shear localization of a crust-upper mantle system with nonlinear viscoelastic material. *Journal of Geophysical Research: Solid Earth*, *123*, 9269–9285. https://doi.org/10.1029/2018JB016421

Received 19 JUL 2018
Accepted 21 SEP 2018
Accepted article online 26 SEP 2018
Published online 29 OCT 2018

Abstract We investigate the evolution of tectonic background stress and elastic as well as inelastic strain in a crust-upper mantle system around an infinitely long vertical strike-slip fault in a self-consistent mechanical earthquake cycle model. In the early stage of the stress evolution, deformation of the crust and the upper mantle is dominated by a uniform simple shear. Shear localization in the lower crust starts when coseismic rupture extends to the entire brittle upper crust. Together with this transition, the earthquake recurrence intervals decrease by an order of magnitude due to a basal drag originated from a localized plastic flow of the lower crust. After the shear zone is fully developed in the lower crust, the fault slip rate catches up with the far-field velocity and earthquakes starts to occur periodically. Such a steady state can be reached in several hundred thousand years from the beginning, which includes few hundreds of earthquake cycles. A shear zone with large cumulative strain needs a few million years to develop under an intraplate strike-slip fault, which is much longer than the time for shear strain rate to be localized. The model successfully reproduced evolution of tectonic stress around an intraplate strike-slip fault, interacting with the development of localized shear zone in the lower crust. The model demonstrates the importance of considering the whole mechanical system in which rheological structure and fault activities interacting with each other for the better understanding of the intraplate earthquakes.

1. Introduction

It is generally accepted that the upper crust of the Earth deforms in an elastic/brittle manner, while ductile flows accommodate regional deformation in the lower crust (e.g., Kohlstedt et al., 1995; Sibson, 1982). However, it is still not well understood what role the elastic/brittle and plastic deformation plays and how they interact with each other in the crustal deformation. Previous studies proposed two end-member models for the deformation around an interplate strike-slip fault. One is the basal drag model, which postulates the upper crust passively follows the distributed flow of the stronger plastic lower crust (Bourne et al., 1998). The other is the viscoelastic coupling model (Savage & Prescott, 1978), which considers the time-dependent deformation around a strike-slip fault zone as a combined result of far-field loading, earthquake rupture on the fault, and stress relaxation in the viscoelastic substratum under the fault. Both models reproduce the observed deformation pattern around a vertical strike-slip fault strands equally well (Savage et al., 1999), which means that geodetically observed interseismic deformation alone cannot resolve the problem. On the other hand, geophysical observations such as seismic reflection/refraction surveys provide constrain on the deformation in the lower crust. Again, opinions are divided as some studies show that Mohorovicic (Moho) offsets under a strike-slip fault (e.g., Henstock et al., 1997; Zhu, 2000), implying that the fault cuts through the entire crust, while others show that Moho depth vary rather smoothly across the fault zone, indicating that deformation in the lower crust is broadly distributed (e.g., Weber et al., 2004; Wilson et al., 2004).

Compared to interplate faults, intraplate strike-slip faults are characterized by much slower long-term slip rates. However, geophysical observations such as the seismic tomography (Nakajima & Hasegawa, 2007; Nakajima et al., 2010; Wittlinger et al., 1996) and magnetotelluric surveys (Ogawa & Honkura, 2004; Yoshimura et al., 2009) indicate localized weak structures in the lower crust under the fault, which suggest the existence of a localized shear zone. It is impossible to directly resolve the ongoing deformation of the lower crust, but highly sheared rocks such as mylonite found in exhumed fault zones provide direct evidence for localized lower crustal deformation in the past.

To understand physical mechanisms of shear zone formation in the lower crust, different shear strain concentration mechanism such as shear heating (Leloup et al., 1999; Thatcher & England, 1998) and power law creep (Takeuchi & Fialko, 2012) were proposed. Various observations indicate shear localization occurs even under a very low slip rate condition of intraplate faults. Zhang and Sagiya (2017) investigated physical mechanism of shear zone formation under a slow slip rate condition and concluded that the power law rheology plays the principal role; however, the formation of shear zone was not modeled in that study. As the stress propagates in the material with nonlinear (power law) rheology (Melosh, 1976), it is important to understand the evolution of shear stress and strain distribution in the crust.

In the previous studies using rheological laws to simulate the lower crustal deformation under the San-Andreas Fault (SAF), a thermal mechanical model showed that steady state deformation under an interplate strike-slip fault can be reached in a few million years (e.g., Leloup et al., 1999; Takeuchi & Fialko, 2012; Thatcher & England, 1998) much shorter than the history of the SAF (Atwater, 1970). In the recent few millions of years, the slip rate of the SAF is stable (DeMets & Dixon, 1999) and it is consistent with the geodetic estimation (Bourne et al., 1998). Therefore, the time-dependent solution was not considered in these studies.

On the other hand, for intraplate strike-slip fault, geologically estimated slip rates are often slower than the geodetic estimations (e.g., Herbert et al., 2014; Ohzono et al., 2011). Gourmelen et al. (2011) interpreted this discrepancy as an evidence for the acceleration of an evolving strike-slip fault. However, the existence of such fault slip acceleration, and its possible mechanisms are still unclear.

In order to understand the evolution of the shear stress, effective viscosity and deformation around an infinitely long strike-slip fault with constant tectonic loading in the far field on an initially unstressed crust-mantle system. We construct a two-dimensional self-consistent mechanical model to simulate evolution processes. In this model, we assume the entire system is composed of nonlinear Maxwell material whose plastic flow follows experimental rheological laws and the occurrence of earthquakes is stress controlled. We show how structures including the fault in the upper crust and the shear zone in the lower crust and the upper mantle are developed with the evolution of shear stress and how these processes depend on boundary conditions and rheological properties. We also discuss how shear zone evolution affects the result of geodetic, geological, and geophysical observations.

2. Model Description

We simulate the deformation of the crust-mantle system by applying a constant velocity to represent far-field loading. We consider the earthquake cycle by solving the stress equilibrium equation for stress changes in the interseismic and coseismic period in a two-dimensional plane perpendicular to a vertical strike-slip fault trace. All numerical calculations presented in this study were performed using MATLAB Partial Differential Equation Toolbox accelerated by graphics processing unit.

2.1. Model Geometry

We consider the deformation of the crust-mantle system around an infinitely long vertical strike-slip fault, as shown in Figure 1. We consider a two-dimensional problem so that displacements occur only in the fault-parallel direction. Considering the symmetry of the vertical strike-slip fault, we consider that only one side of the fault is bounded by the surface and a vertical plane of bilateral symmetry that represents the fault plane. The model domain is 65 km thick in the vertical (z) direction and 50 km wide in the fault normal (x) direction being composed of 35-km-thick crust and 30-km-thick mantle layers divided by the horizontal Mohorovicic discontinuity (Moho).

2.2. Temperature Profile

The temperature profile in this study is defined by the thermal model considering the radioactive heat production in the crust (Sclater et al., 1980)

$$T(z) = \begin{cases} \frac{Q_r z}{k_1} + \frac{D^2 A_0}{k_1}\left(1 - \exp\left(-\frac{z}{D}\right)\right) & (z \le h)\,, \\ T(h) + \frac{z-h}{k_2} Q_r & (z > h)\,, \end{cases} \tag{1}$$

where h is the depth of the Moho, and k_1 and k_2 are the thermal conductivity of the crust and the upper mantle, which are assumed to be 2.6 $W{\cdot}K^{-1} \cdot m^{-1}$ and 2.5 $W{\cdot}K^{-1} \cdot m^{-1}$, respectively. Q_r is the heat flow at the

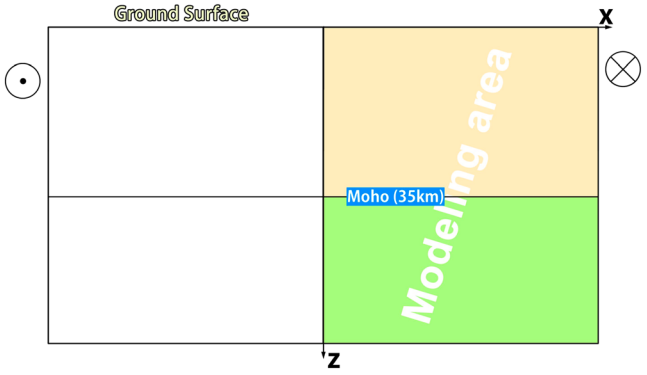

Figure 1. Model geometry. Moho = Mohorovicic discontinuity.

base of the model, D characterizes the degree of upward migration of the radiogenic elements, and A_0 is the heat production at the surface, which is given by

$$A_0 = (Q_0 - Q_r)/D, \tag{2}$$

where Q_0 is the heat flow on the ground surface, which is assumed to be 65 mW/m^2. By fixing the temperature at the bottom of the model, 1150 °C in this study, Q_r and D can be solved from equations (1) and (2). We do not consider the effect of shear and frictional heating in this study in both intraplate and interplate cases. In the case of intraplate strike-slip fault, only a small amount of heat is generated on intraplate strike-slip, which has almost no influence on the intraplate deformation (Zhang & Sagiya, 2017). In the case of an interplate strike-slip fault, a considerable amount of heat is generated, which has a significant effect on the degree of shear concentration in the lower crust in the timescale of several million years (e.g., Takeuchi & Fialko, 2012; Thatcher & England, 1998). On the other hand, this study simulates fault evolution for less than ~1 million years, which is too short for dissipated heat to have a notable influence on the deformation of the shear zone under an interplate strike-slip fault. Therefore, the effect of shear and frictional heating is not considered even in the case of interplate strike-slip fault.

2.3. Rheologies

We assume that the entire crust and the upper mantle is composed of nonlinear Maxwell viscoelastic materials. Shear strain rate of the Maxwell material is represented as a sum of elastic shear strain rate and viscous shear strain rate due to a plastic flow.

$$\dot{\varepsilon}^T = \dot{\varepsilon}^v + \dot{\varepsilon}^e = \frac{\tau}{\eta_{eff}} + \frac{1}{G}\frac{\mathrm{d}\tau}{\mathrm{d}t}, \tag{3}$$

where $\dot{\varepsilon}^T$ is the total shear strain rate; $\dot{\varepsilon}^v$ and $\dot{\varepsilon}^e$ are the viscous and elastic shear strain rate, respectively; and G is the elastic shear modulus, which is assumed to be 30 GPa for the entire model. η_{eff} is the effective viscosity, which can be calculated from shear stress (τ) using the constitutive relation for the plastic flow of rocks as follows (e.g., Bürgmann & Dresen, 2008):

$$\dot{\varepsilon}^v = A\tau^n L^{-m} f_{H_2O}^r \exp\left(-\frac{Q+pV}{RT}\right), \tag{4}$$

where τ_s is the maximum shear stress given by the square root of the second deviatoric stress invariant; L is the grain size; f_{H_2O} is water fugacity; Q and V are activation energy and activation volume, respectively; R is the universal gas constant; p is pressure; and A, n, m, r, are material constants. Water fugacity is calculated with the van der Waals equation (Karato, 2012). The detailed calculation method can be found in Zhang and Sagiya (2017).

For the rheological model, we assume wet quartz (Rutter & Brodie, 2004) or wet anorthite (Rybacki et al., 2006) for the crust and wet olivine (Hirth & Kohlstedt, 2013) for the upper mantle (Table 1). The laboratory-derived parameters of experimental flow laws are summarized in Table 2. Regarding the physical mechanism of plastic flow, in this study, we only consider dislocation creep since the evolution of the plastic shear zone is mainly controlled by grain size insensitive dislocation creep (Zhang & Sagiya, 2017). For comparison, we also test a case of a stress independent linear rheology with a fixed viscosity structure depending on the temperature.

2.4. Earthquake Cycle Model

Our numerical simulation starts from a stress-free initial condition. Far-field velocity v_0 is assumed as a half of the long-term fault slip rate, which is assumed to be 1 and 30 mm/year for intraplate and interplate faults (Table 1), respectively. At each time step, the stress on the fault is compared with the fault strength to judge if there occurs an earthquake (Figure 2). If the stress is smaller than the strength over the entire fault, we calculate the stress change for a small time step caused by the far-field motion. During the interseismic period, the fault is locked and no incremental displacement occurs at $x = 0$ km. The traction-free condition, that is, $\tau_{yz} = 0$, is applied on the ground surface and at the bottom of the model at the depth of 65 km. Shear stress accumulates on the fault until the Coulomb failure criterion is satisfied:

Table 1
Model Configurations

Model	Crustal rheology	Fault frictional coefficient	Boundary velocity (mm/year)
Q1W	Wet quartz	0.2	1
A1W	Wet anorthite	0.2	1
Q1S	Wet quartz	0.6	1
A1S	Wet anorthite	0.6	1
Q30W	Wet quartz	0.2	30
Q30S	Wet quartz	0.6	30
Linear	Prescribed viscosity structure	0.2	1

Seven model configurations were tested by this study. The nomenclature of the model configuration is as follows: The first letter denotes rheological model (A, anorthite; Q, quartz). The rheological parameters for anorthite and quartz are summarized in Table 2. The last letter denotes fault strength (W, weak; S, strong). The number between two letters denotes the total relative velocity in millimeters per year.

$$\tau_f = \mu_f \sigma_n + C_f, \tag{5}$$

where C_f is the frictional cohesive strength, which is assumed to be 5 MPa in this study, σ_n is the fault normal stress given by ρgh, and μ_f is the coefficient of internal friction, which is assumed to be 0.2 for the weak fault and 0.6 for the strong fault (Table 1).

The stress in the crust and the upper mantle is calculated from the accumulated elastic strain, which is the product of elastic strain rate and time. In the calculation of elastic strain change in a small time step, we assume that elastic ($\dot{\varepsilon}_{ij}^{e}$) and viscous ($\dot{\varepsilon}_{ij}^{v}$) shear strain rates are constant during the time step. By solving the time-dependent differential equation (equation (3)) for shear stress, we obtain the expression for the shear stress at time $t_0 + \Delta t$:

$$\tau_{ij}^{t_0+\Delta t} = \tau_{ij}^{t_0} + G\left(\dot{\varepsilon}_{ij}^{t_0} - \frac{\tau_{ij}^{t_0}}{\eta_{\text{eff}}}\right)\Delta t, \tag{6}$$

where $\tau_{ij}^{t_0}$ is the shear stress at time t_0. Adaptive time step Δt is determined by the minimum effective viscosity of the whole system ($\eta_{\text{eff}}^{\min}$), that is, $\Delta t = 0.1\eta_{\text{eff}}^{\min}/G$. Since the effective viscosity and total viscous shear strain rate are the function of stress (equations (3) and (4)) at each time step, they can be calculated from shear stress using equation (4). The total shear strain rate in equation (6) can be obtained by solving the stress equilibrium equation

$$\frac{\partial \tau_{yx}}{\partial x} + \frac{\partial \tau_{yz}}{\partial z} = 0. \tag{7}$$

In the coseismic period, the static stress drop is applied on the fault and its deep extension is locked. The traction free condition, that is, $\tau_{yz} = 0$ and $\tau_{yx} = 0$, has been applied to both horizontal boundaries and the far-field boundary.

Because the entire model behaves elastically in the coseismic period, there is a linear relationship between the stress and the strain changes, that is,

Table 2
Rheological Properties of Rocks From Laboratory Measurements

Rock type		log$A$ ($\text{MPa}^{-n-r}\mu\text{m}^{m}\text{s}^{-1}$)	n	Q (kJ/mol)	m	r	V (cm^3/mol)	Ref.
Wet quartz	disl.[a]	−4.9	3	242	0	1	0	Rutter and Brodie (2004)
Wet anorthite	disl.[a]	0.2	3	345	0	1	38	Rybacki et al. (2006)
Wet olivine	disl.[b]	3.2	3.5	520	0	1	22	Hirth and Kohlstedt (2013)

disl. denotes dislocation creep. Density of quartz, anorthite, and olivine are 2,660, 2,760, and 3,214 kg/m^3,respectively.

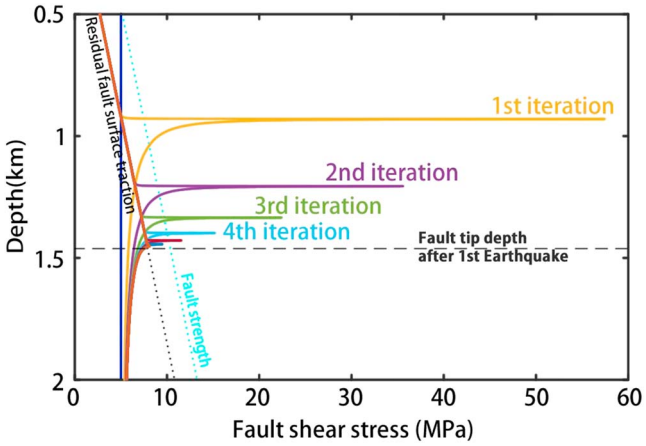

Figure 2. Stress concentration at the crack tip can be eliminated by several iterations. Time does not proceed in these iterations.

$$\Delta\tau_{ij} = G\Delta\varepsilon^{e}_{ij}. \tag{8}$$

The elastic shear strain change ($\Delta\varepsilon^{e}_{ij}$) can also be obtained by solving the stress equilibrium equation (equation (7)).

We calculate the stress change using the stress boundary condition given by the difference between stress on the fault in the previous step and the residual fault surface traction (black line). When a brittle fracture occurs in the upper crust, stress concentrates near the crack tip, the deepest point of the rupture. In order to eliminate the stress concentration near the crack tip, we apply an iterative method, which is illustrated in Figure 3. The dark-blue line is the stress on the fault before the first rupture, and other solid lines show the stress on the fault after each iteration. Iteration of coseismic deformation continues until stress concentration at the crack tip becomes negligibly small. As a result, the fault tip depth increases after each earthquake. These iterations are considered as an instantaneous process to represent coseismic change in our simulation.

After repeating several times, the fault can penetrate the entire upper crust and the brittle-ductile transition zone (BDTZ), where the failure mode changes from brittle fracture to plastic flow (Kohlstedt et al., 1995). Starting from an initially stress-free condition, the temporal evolution of stress and strain distribution is calculated until the appearance of a regular earthquake cycle, in which shear stress distribution does not evolve over each earthquake cycle any more. Based on the definition of the brittle-ductile transition (Kohlstedt et al., 1995), the depth range of BDTZ can be quantitatively estimated from the distribution of coseismic offsets on the fault after the regular earthquake recurrence started. In this study, we tentatively define BDTZ as the depth range where the modeled coseismic slip decreases from 90% of its maximum value at the surface to 0.

Model configurations considered in this study are summarized in Table 1. Except for the linear viscosity case, other cases are referred using a number between two letters. The first letter indicates the rock rheology (A, anorthite; Q, quartz) of the crust, and the second letter indicates the fault strength (W, $\mu_f = 0.2$; S, $\mu_f = 0.6$). The number between two letters indicates the total relative velocity ($2v_0$) in millimeters per year. In this paper, we refer to each case by the name shown in Table 1.

3. Results

In this section, we present a spatiotemporal evolution of shear stress, effective viscosity, viscous shear strain rate, and the shear strain associated with the intraplate strike-slip fault. Each snapshot is taken at the end of

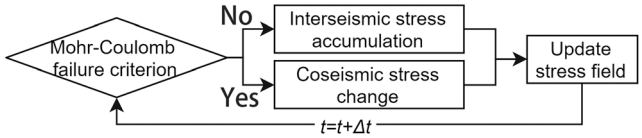

Figure 3. The algorithm for calculation of the earthquake cycle, both interseismic and coseismic stress change is solved using stress equilibrium equation (equation (7)).

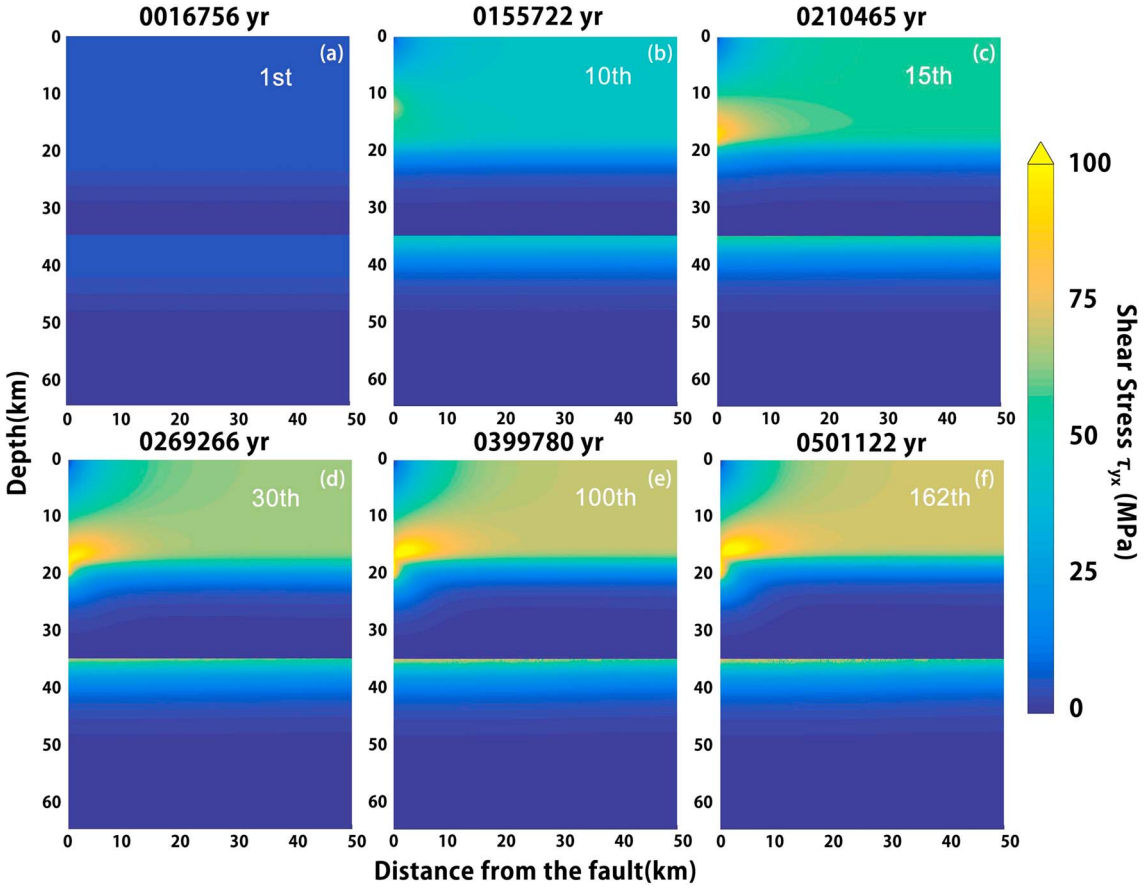

Figure 4. Shear stress τ_{yx} evolution in the model of Q1W. Each figure is plotted right before an earthquake, the number of earthquake cycle is shown in each figure, and the elapsed time is shown on the top of each figure.

the interseismic period in earthquake cycles. Next, we show the evolution of the fault behavior by showing the shear stress accumulation rate averaged over different earthquake cycles, the coseismic slip, and the shear stress on the fault plane. Among seven different cases (Table 1), we only show the evolution process in the case of Q1W because the scenario of the evolution is similar in the cases with different rock rheology and boundary conditions. After the regular earthquake recurrence starts (i.e., shear stress distribution does not change from cycle to cycle), we show the results for all seven cases because the distributions of shear stress, viscous shear strain rate, and effective viscosity depend on model configurations.

3.1. Evolution of Shear Stress

Figure 4 shows the stress evolution of the model Q1W. Starting from a non-stressed condition, shear stress increases in the crust and the upper mantle due to far-field loading. The effective viscosity is inversely proportional to the shear stress with a power of $n - 1 (n = 3)$. At the beginning, the stress increases linearly in time at a constant rate of ~300 Pa/year because the effective viscosity of the non-stressed material is infinitely large and the whole model area behaves elastically (Figure 4a). In the elastic layer, the shear stress uniformly increases until the stress on the fault reaches the fault cohesive strength (5 MPa). As earthquakes repeat, the stress gradually becomes localized around the fault tip. Figure 4b shows the shear stress distribution before the 10th earthquake (0.15 Myr), the shear stress near the fault tip is ~70 MPa, which is higher than the stress in the far field (~50 MPa). At 0.21 Myr (Figure 4c), the fault tip reach the BDTZ. After that, the change of the shear stress over earthquake cycles becomes smaller. The increase of the maximum shear stress from 0.21 to 0.27 Myr (Figure 4d) is only about 4.7 MPa, which is much smaller than the maximum shear stress increase of 24.4 MPa from 0.15 to 0.21 Myr. Around 0.40 Myr, the shear stress stops evolving and a regular recurrence of earthquakes starts (Figure 4f).

In the far field, the shear stress gradually increases with time until the regular recurrence starts. After that, the shear stress in the far field gets as large as ~70 MPa even at the ground surface. Such high shear stress value

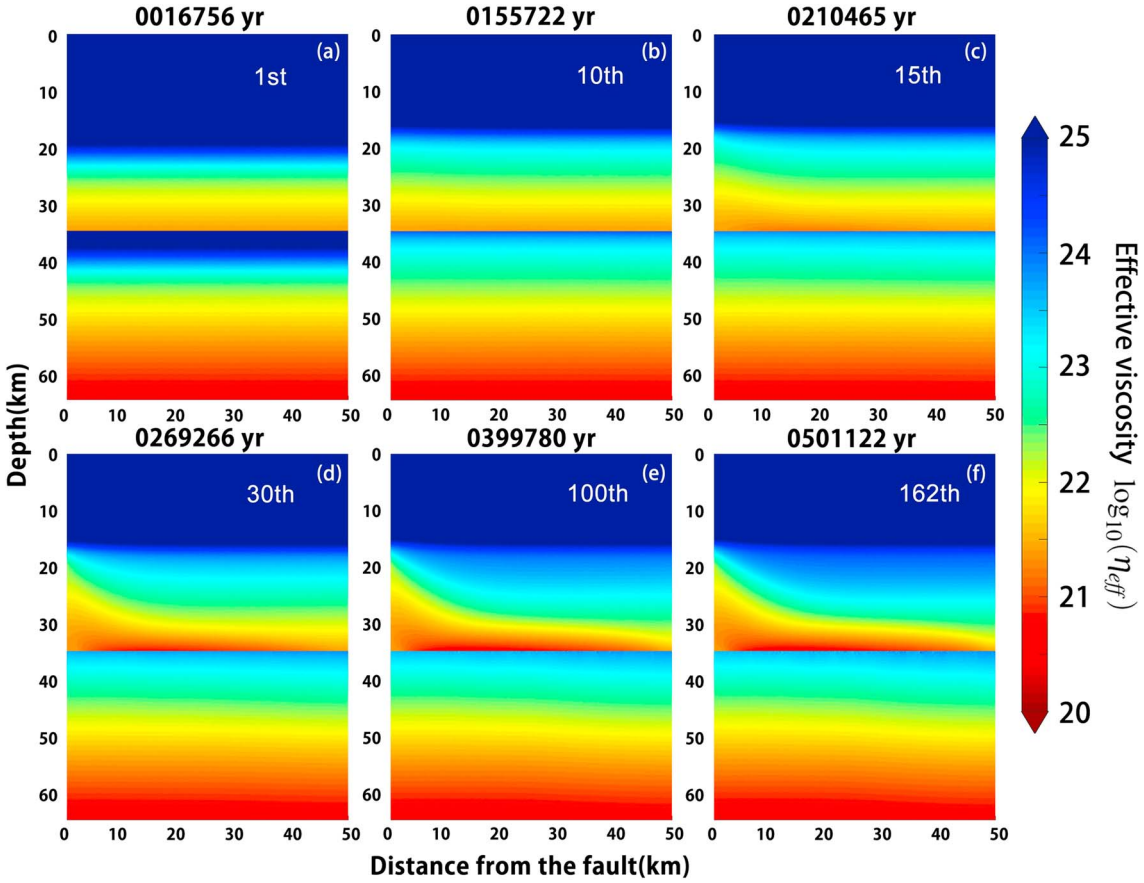

Figure 5. The effective viscosity η_{eff} evolution in the model of Q1W. Each figure is plotted right before an earthquake, the number of earthquake cycle is shown in each figure, and the elapsed time is shown on the top of each figure.

is not realistic in the Earth's crust, especially for the shallower part where the rock strength is small. Such a consequence is caused by our assumption that the whole model area is composed of a Maxwell viscoelastic material. The upper crust behaves elastically because of its low temperature. In the future studies, off-fault plasticity in the upper crust should be considered to limit the stress in the upper crust.

3.2. Evolution of Effective Viscosity

Figure 5 shows the evolution of the effective viscosity structure. Before the fault tip reaches the deeper part of the lower crust (Figures 5a and 5b), the effective viscosity in the lower crust and the upper mantle has a layered structure and there is a sudden change of effective viscosity at the depth of Moho. As the fault tip is getting closer to the lower crust (Figures 5c and 5d), the effective viscosity starts to drop near the fault due to the shear stress concentration. At the same time, the effective viscosity in the deeper part of the lower crust also decreases because the shear strain $\dot{\varepsilon}_{yz}$ concentrates above the Moho. In the far field in the lower crust, the effective viscosity increases while the layered structure remains unchanged. After the regular recurrence starts (Figures 5e and 5f) at 0.4 Myr, the structure of effective viscosity does not change any more as the distribution of the effective viscosity at 0.5 Myr are identical to that at 0.4 Myr.

3.3. Evolution of Viscous Shear Strain Rate

Figure 6 shows the evolution of viscous shear strain rate $\dot{\varepsilon}_{yx}$ of model Q1W. Before the fault tip reaches the lower crust, the deformation of the lower crust and the upper mantle are dominated by a laminar flow in which the viscous shear strain rate is about 10^{-16} s^{-1}. The deformation starts to concentrate under the fault at 0.2 Myr when the fault tip reach the BDTZ. At the same time, the shear strain rate in the far field of the lower crust decreases. Under the elastic upper crust at the depth of 17–20 km, there is a thin layer where the shear strain rate does not change after the 10th earthquake because the effective viscosity in that layer is larger than 10^{24} Pa and the Maxwell relaxation time ($t_r = \eta_{\text{eff}}/G$) is longer than 1 Myr. Since the time span of our simulation is less than 1.6 Myr, stress of this layer cannot be relaxed. Compared with the deeper part

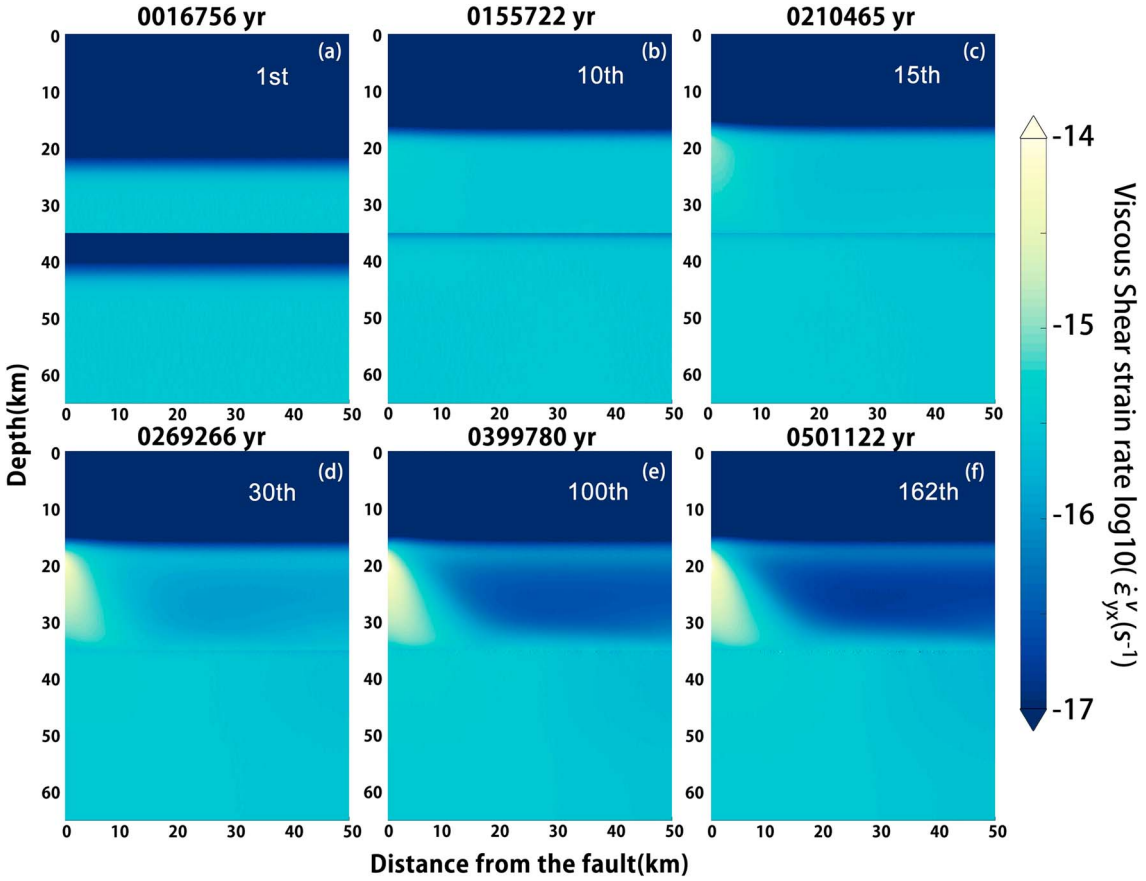

Figure 6. The viscous shear strain rate $\dot{\varepsilon}_{yx}$ evolution in the model of Q1W. Each figure is plotted right before an earthquake, the number of earthquake cycle is shown in each figure, and the elapsed time is shown on the top of each figure.

of the lower crust, the degree of shear strain concentration in the upper mantle is much smaller, because the effective viscosity of the shallowest part upper mantle is $\sim 10^4$ times larger than that in the deepest part of the lower crust (Figure 5).

3.4. Evolution of Shear Strain

Figure 7 shows the evolution of total shear strain in model Q1W. In the upper crust, the distribution of the strain has a similar pattern as the distribution of the shear stress because the strain is linearly proportional to the shear stress. In the lower crust under the fault, the distribution of shear strain is a temporal integration of the viscous shear strain rate shown in Figure 6. After the regular earthquake recurrence started, the distribution of the shear strain in the lower crust shares the same characteristics with the distribution of the viscous shear strain rate. In the crust, there is no discontinuity between the upper and the lower crust and in the far field, the maximum shear strain of the crust reaches $\sim 2.5 \times 10^{-3}$. On the other hand, the strain discontinuity between the crust and the upper mantle is obvious because there is almost no strain concentration in the upper mantle.

3.5. Evolution of the Fault Behavior

In the process of the tectonic stress evolution, the fault behavior changes in time. Figure 8 shows the evolution of the averaged interseismic stressing rate (a), coseismic offset on the fault in an earthquake cycle (b), and shear stress on the fault (c). Before the first earthquake, the shear stress is less than 5 MPa and increases not only in the upper crust but also in the shallower part of the lower crust (red line in Figure 8a). Because the built-up stress is a result of a constant far-field loading, the stressing rate is nearly a constant at 300 Pa/year.

As the stress increases, deeper part of the crust with a higher strength starts to break in earthquakes. After a few earthquake cycles, earthquakes start to break through a large portion of the elastic upper crust (e.g., coseismic offset of the 10th earthquake is shown by the green line in Figure 8b). Before the fault reaches the deeper part of the upper crust, the stressing rate in the upper crust is nearly a constant, which, in this case, is 20

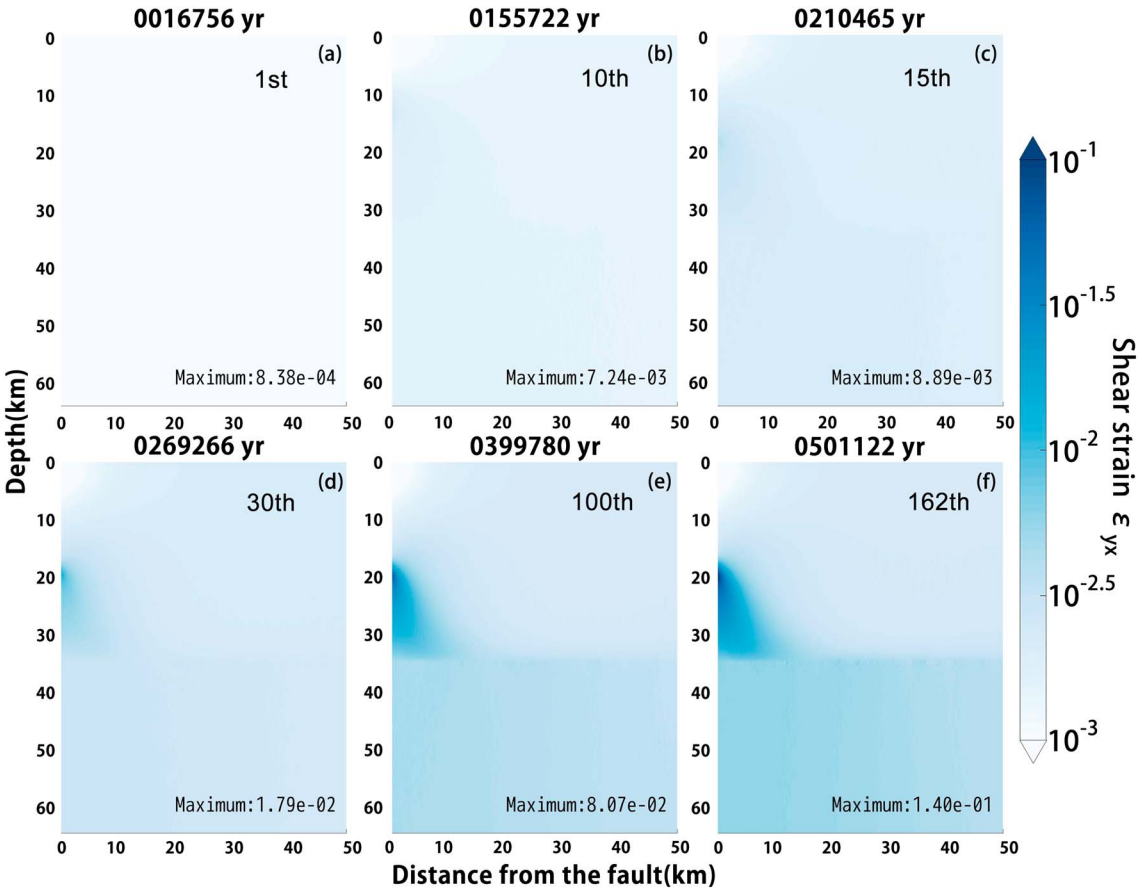

Figure 7. The viscous shear strain rate $\dot{\varepsilon}_{yx}$ evolution in the model of Q1W. Each figure is plotted right before an earthquake, the number of earthquake cycle is shown in each figure, and the elapsed time is shown on the top of each figure.

to 40 Pa/year larger than the initial stressing rate. The increase of the stressing rate is a result of the basal drag in the lower crust. In the shallower part of the lower crust, the stress starts to decrease due to stress relaxation.

After the fault tip reaches the depth of BDTZ, the stressing rate in the upper crust and the shallowest part of the BDTZ increases due to the basal drag (blue line in Figure 8a). As the fault gets closer to the lower crust, the effect of the basal drag becomes more intense after each earthquake. The averaged interseismic stressing rate significantly increases in the deeper part of the upper crust and the shallow part of BDTZ. In the shallow part of the upper crust, the stress perturbation is smaller than at the shallow part of BDTZ. After the regular earthquake recurrence started, the maximum shear stressing rate is ~3 kPa/year at the depth of ~18 km, which is 6 times larger than that on the surface (~0.5 kPa/year). Because the fault is mainly loaded by the basal drag, the coseismic offsets increment toward the ground surface is small and the offset value on the ground surface is equal to the far-field travel distance during an interseismic period after regular earthquake recurrence started.

The coseismic offsets after the regular recurrence starts can be used to quantitatively estimate the depth range of BDTZ. In Figure 8 gray broken lines indicate the upper and lower boundaries of the BDTZ. In the case of Q1W, the depth of BDTZ ranges from 17.6 to 20.4 km. In other cases considered in this study, the depth of BDTZ can be estimated in the same manner and the results, which are summarized in Table 3, depend on the assumptions of rock rheology, far-field velocity, and fault strength.

3.6. Effect of Model Configurations

In this study, seven different cases, including one linear case with stress-independent layered viscosity structure, have been considered (Table 1) to understand how rock rheologies, far-field velocities, and fault strength affect the evolution process of stress, deformation, and effective viscosity structure around the vertical strike-slip fault. Figures 9 and 10 show the shear stress, effective viscosity, and viscous shear strain rate of

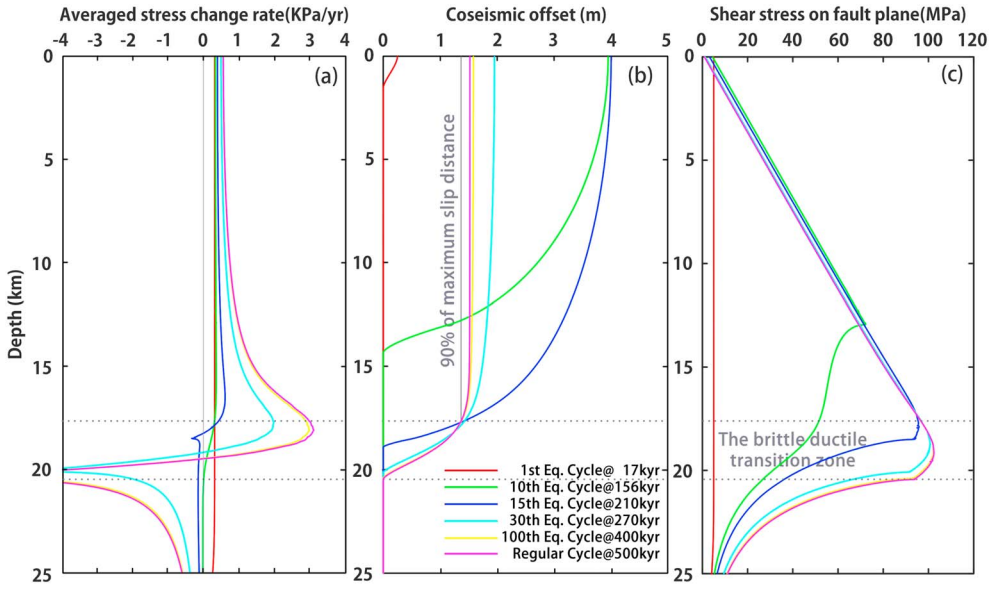

Figure 8. Stress change rate averaged over an earthquake cycle (a), coseismic offset (b), and shear stress on fault plane right before an earthquake (c). Lines with different colors indicate the result from earthquakes at different time. The gray broken lines indicate the depth of brittle-ductile transition zone.

intraplate and interplate cases. Each of these figures is plotted at the end of an interseismic period. Time to reach regular recurrence for each case is summarized in Table 3.

In our model, the magnitude of the shear stress in the bulk of the crust and the upper mantle is largely influenced by the fault strength. The shear stress reaches its maximum at the depth of BDTZ. Because the fault strength is assumed to linearly depend on the depth, the deeper the BDTZ is, the larger the magnitude of shear stress in the BDTZ. The assumption of rock rheology has a significant influence on the depth of the BDTZ. Compared to the cases with wet quartz, the depth of BDTZ is ~6 km deeper in the cases with wet anorthite (Table 3). Therefore, the shear stress in the cases with wet quartz (Figures 9a and 9c) is smaller than that in the cases with wet anorthite (Figures 9b and 9d). On the other hand, the depth of BDTZ in the cases of intraplate cases are only ~2 km shallower than that in the interplate cases (Table 3). In the nonlinear cases, because we assume a power law rheology for the entire model, the viscous shear stress in the lower crust is proportional to shear strain rate with a power of $1/n(n = 3)$. Therefore, the shear stress is less sensitive to the shear strain rate. In the shear zone under the fault, shear stress in the interplate cases is ~3 times larger than intraplate cases.

Unlike the shear stress, viscous shear strain rate in the shear zone linearly depends on the far-field velocity. For the intraplate cases (Figures 9k–9o) and the interplate cases (Figures 10e–10f), the maximum shear strain rates are $\sim 1.7 \times 10^{-14}\,s^{-1}$ and $\sim 4.6 \times 10^{-13}\,s^{-1}$, respectively. Because the effective viscosity is inversely proportional to the stress with a power of $n - 1$ ($n = 3$), the effective viscosity of the lower crust in the inter-

Table 3
Model Properties After Regular Recurrence Starts

Model	Depth of BDTZ (km)	Surface displacement (m)	Recurrence interval (kyr)	Regular recurrence start time (Myr)
Q1W	17.6–20.4	0.76	1.54	0.4
A1W	23.9–27.0	0.84	1.70	0.5
Q1S	15.5–18.0	0.67	1.39	1.0
A1S	21.6–24.5	0.77	1.59	1.4
Q30W	19.7–23.0	0.90	0.061	0.015
Q30S	17.6–20.4	0.78	0.053	0.038
Linear	18.7–23.9	1.23	2.52	0.8

Note. BDTZ = brittle-ductile transition zone.

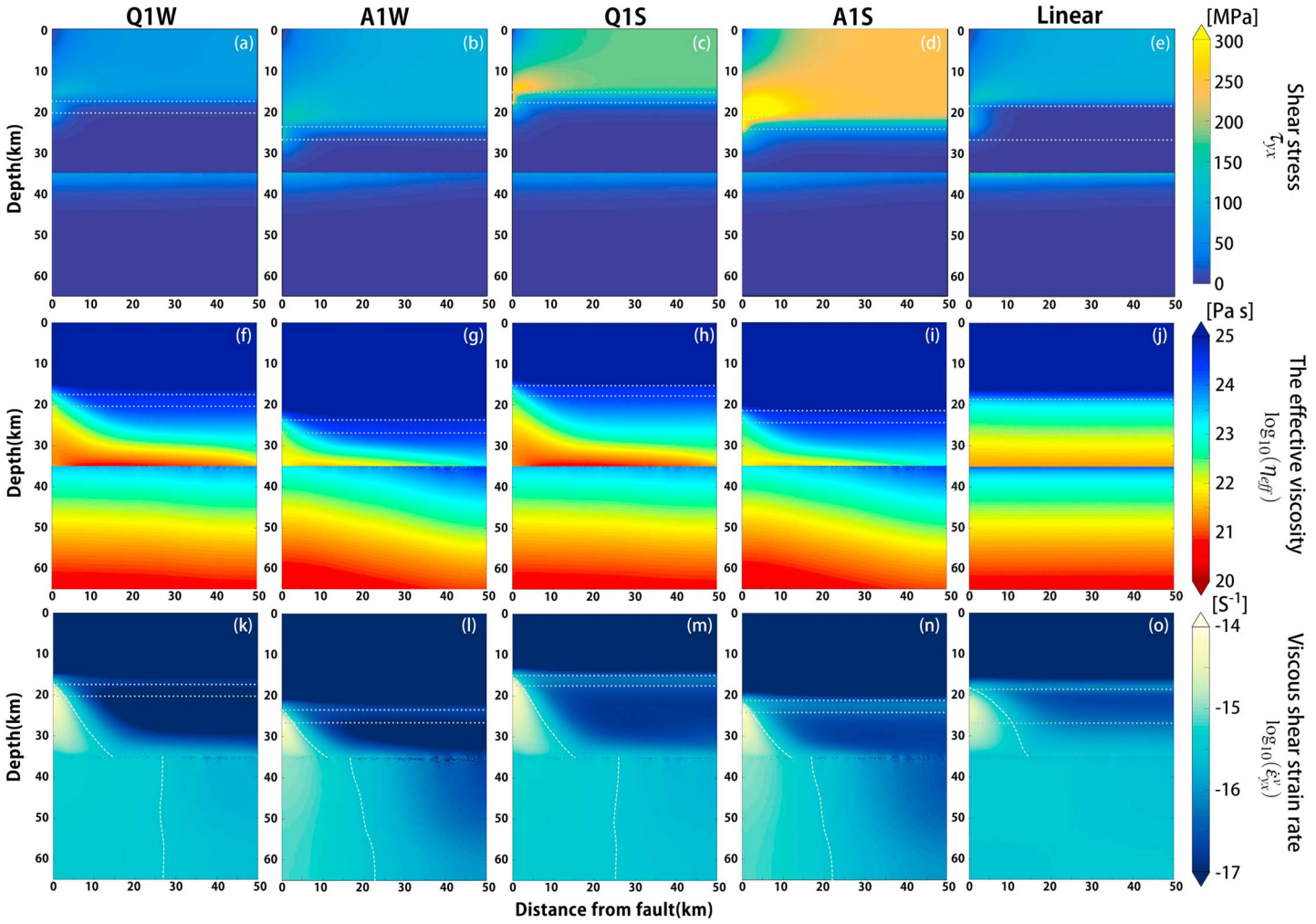

Figure 9. Shear stress (a–e), effective viscosity (f–j), and viscous shear strain rate (k–o) distributions of intraplate cases after regular recurrence is reached. Figures are plotted at the end of an interseismic period right before an earthquake. Each row shows the results of a case, and the name of the case is shown on the top of the row. White broken lines indicate the location where viscous shear strain rate is not changed from the shear strain rate of uniformly distributed simple shear, which is about 3.17×10^{-16} s^{-1} in intraplate cases. The gray broken lines indicate the depth of brittle-ductile transition zone.

plate cases (Figures 9c and 9d) is ~10 times smaller than that in the intraplate cases (Figures 9f and 9g). The maximum shear strain rate in the center of the shear zone is significantly larger than the shear strain rate of uniformly distributed simple shear, which is $\sim 3.2 \times 10^{-16}$ s^{-1} and $\sim 9.5 \times 10^{-15}$ s^{-1} for intraplate and interplate cases, respectively. White broken lines in Figures 9k–9o and 10e–10f indicate the location in the lower crust and the upper mantle where shear strain rate does not change from the beginning when deformation is dominated by uniformly distributed simple shear.

The shear strain rate increase on the left-hand side of the broken line is a result of shear strain concentration. A shear zone with a localized high shear strain develops there. The smaller the distance from the fault to the broken line is, the higher the degree of shear strain concentration. The white broken line enables us to compare the width of the shear zone in different cases. The shear zone width increases with depth, and it is not influenced by the far-field velocity as the location of white broken lines is similar to each other in the cases assuming wet quartz rheology. Compared to the cases of wet quartz rheology, the shear zone of the models with wet anorthite rheology is narrower in the lower crust and the deformation in the upper mantle is more concentrated because of the deeper BDTZ.

In the linear case, the distribution of viscosity is fixed using the effective viscosity structure at the end of the 10th interseismic period of model Q1W (Figure 9j). Because the effective viscosity of Q1W is smaller due to the shear stress concentration, the depth of the bottom of BDTZ is ~ 2.5 km shallower than the linear case. In the

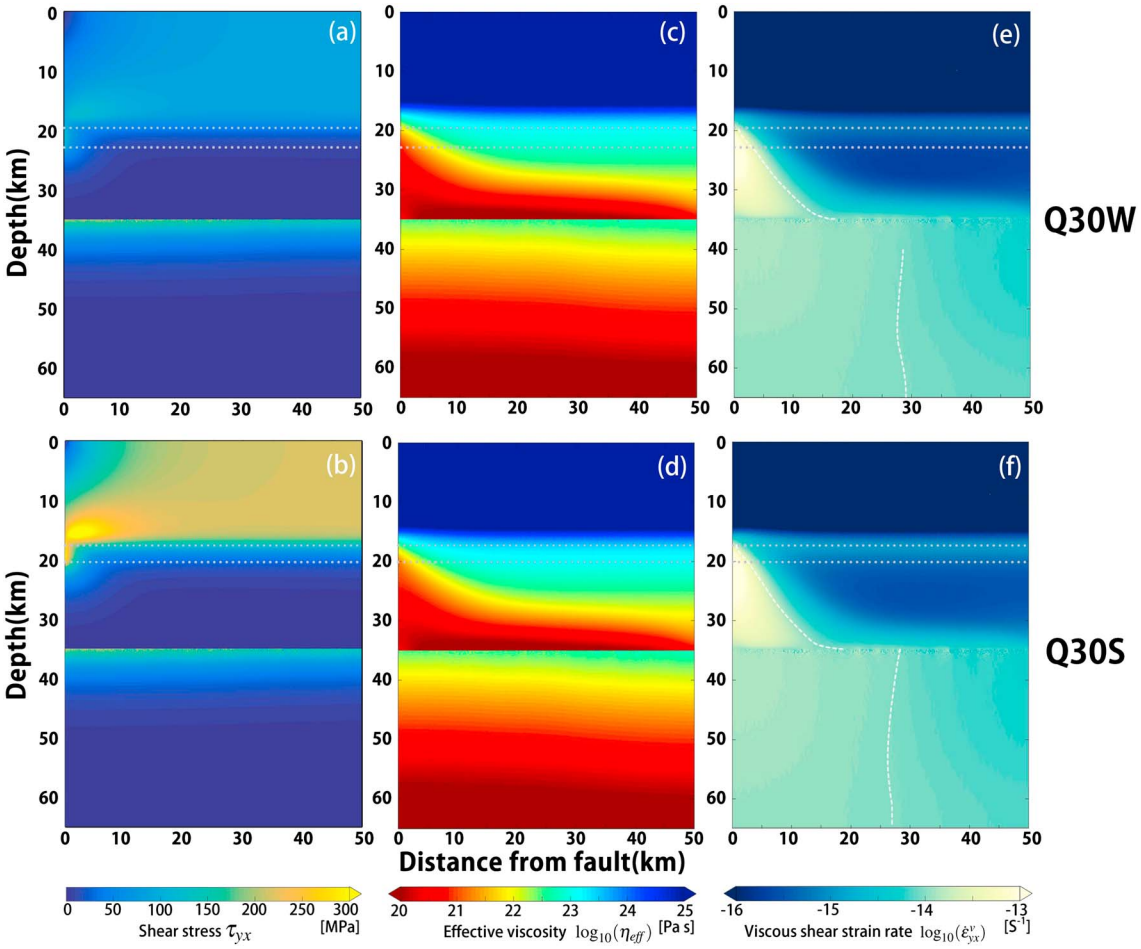

Figure 10. Shear stress (a and b), effective viscosity (c and d), and viscous shear strain rate (e and f) distributions of interplate cases after regular recurrence is reached. Figures are plotted at the end of an interseismic period right before an earthquake. Each column shows the result of a case, and the name of the case is shown at the end of the column. White broken lines indicate the location where viscous shear strain rate is not changed from the shear strain rate of uniformly distributed simple shear, which is about 9.51×10^{-15} s^{-1} in interplate cases. The gray broken lines indicate the depth of brittle-ductile transition zone.

lower crust, because the shear stress concentration is the result of repeating earthquake in the upper crust, the degrees of shear stress concentration are similar to each other in the linear and the nonlinear cases. On the other hand, the deformation is more distributed in the linear case (Figure 9o) compared to Q1W (Figure 9k) because much smaller shear stress is needed for nonlinear cases to achieve the same magnitude of shear strain rate. The maximum shear strain rate in the linear case is $\sim 6.1 \times 10^{-15}$ s^{-1}, which is about one third of the nonlinear case of Q1W.

4. Discussion

4.1. Stage of Fault Evolution

In our simulation results, we find two stages in the fault evolution before regular earthquake recurrence started. The first one is the stress buildup stage. In this stage, the shear stress builds up in the upper crust and the coseismic offsets on the surface increase with the increasing fault tip depth. The second one is the shear localization stage. In this stage, deformation is localized under the fault in the lower crust. Due to the stress relaxation below the upper crust, the stressing rate increases in the upper crust. As a result, the earthquake intervals and the coseismic offsets on the surface decrease with time in the second stage.

Figure 11a shows the time evolution of coseismic offsets in each earthquake for model Q1W. At the beginning of the fault evolution, the slip distance of the first few earthquakes are very small and recurrence intervals of the earthquakes are as long as ~16 kyr. As the stress builds up on the fault, the rupture extends down to the depth of around 10 km. In the stress buildup stage from the beginning to ~0.2 Myr, the coseismic offset of each earthquake on the surface increases in time to the maximum value of 4.4 m. In the shear localization

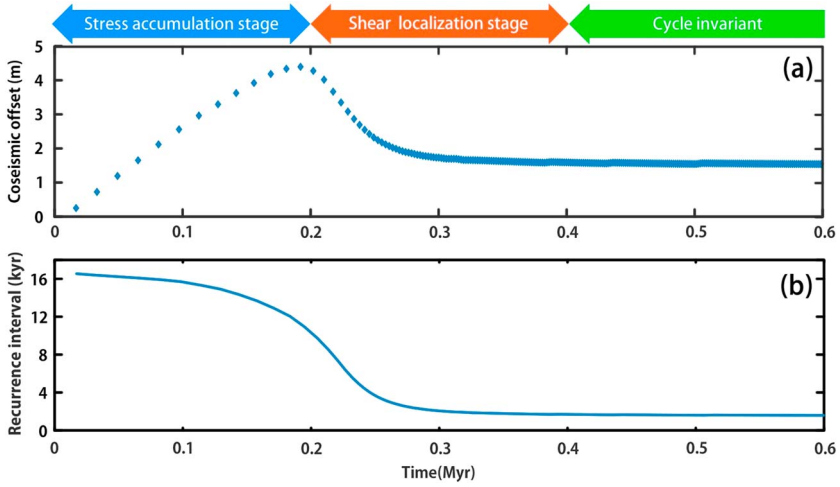

Figure 11. Time evolution of coseismic offset on the surface in each earthquakes (a) and recurrence interval (b) for model Q1W. Each rhombus dots represents an earthquake.

stage from ~0.2 to ~0.4 Myr, the coseismic offsets of each earthquake gradually decrease to 1.54 m. After 0.4 Myr, regular earthquake recurrence starts and the coseismic offset does not change anymore.

Figure 11b shows the time evolution of earthquake recurrence intervals. In the entire process of fault evolution from the beginning to 0.4 Myr, the recurrence interval decreases to 1.54 kyr after regular earthquake recurrence starts. As we have shown in Figure 8, because of the loading from the localized deformation in the lower crust, even with constant far-field loading and fault cohesive strength, the recurrence interval is not a constant in the process of the fault evolution. It decreases with the increasing degree of shear localization in the lower crust. After regular recurrence started, the shear localization occurs under the fault. With continuous loading in the far field, the fault is expected to become recognizable as an active fault because moderate earthquake with total offsets of ~1.5 m occurs every 1,500 years.

For all nonlinear cases in this study, the time duration of two evolution stages are roughly equal each other and the recurrence intervals after regular earthquake recurrence starts are about one tenth of the recurrence intervals at the beginning. On the other hand, for the linear case, the time duration of the shear localization stage is ~0.6 Myr. Compare to the case of Q1W, which is the counterpart of the linear case, the time duration of the shear localization stage in the linear case is much longer. Because the shear strain rate linearly depends on the shear stress in the linear case, the increment of the shear strain rate after each earthquake is smaller in the linear case. For all the cases in this study, time to reach regular recurrence are summarized in Table 3.

4.2. Time to Develop a Ductile Shear Zone

The magnitude of shear strain in the lower crust is directly related to the cumulative offsets on the surface. Our results suggest that heterogeneous structures are expected to be more obvious under a strike-slip fault with a larger cumulative offset. Zhu (2000) showed that Moho offsets are more obvious under the SAF in southern California compared to that under the eastern California shear zone. For other major continental strike-slip fault, such as the Alpine Fault in New Zealand, the North Anatolian Fault in Turkey, and the Altyn Tagh Fault in Tibet, heterogeneous seismic velocity structures has also been revealed by geophysical observations, which indicates that shear zone do exist in the lower crust under the fault (e.g., Elvira et al., 2017; Stern et al., 2007; Wittlinger et al., 1998). Shear zones under these faults are well developed because the cumulative offsets of these faults range from several tens of kilometers to several hundreds of kilometers (Cowgill et al., 2003; Stirling et al., 1996).

Intraplate strike-slip faults need a much longer time until a shear zone develops under them. Such shear zones in the lower crust may not be visible by geophysical observations for most of intraplate faults. However, shear localization under the fault starts at an early stage of the deformation (Figure 12). In the case of A1S it takes ~0.7 Myr to start localized deformation in the lower crust, which is the latest among all four nonlinear cases with a boundary velocity of 0.5 mm/year.

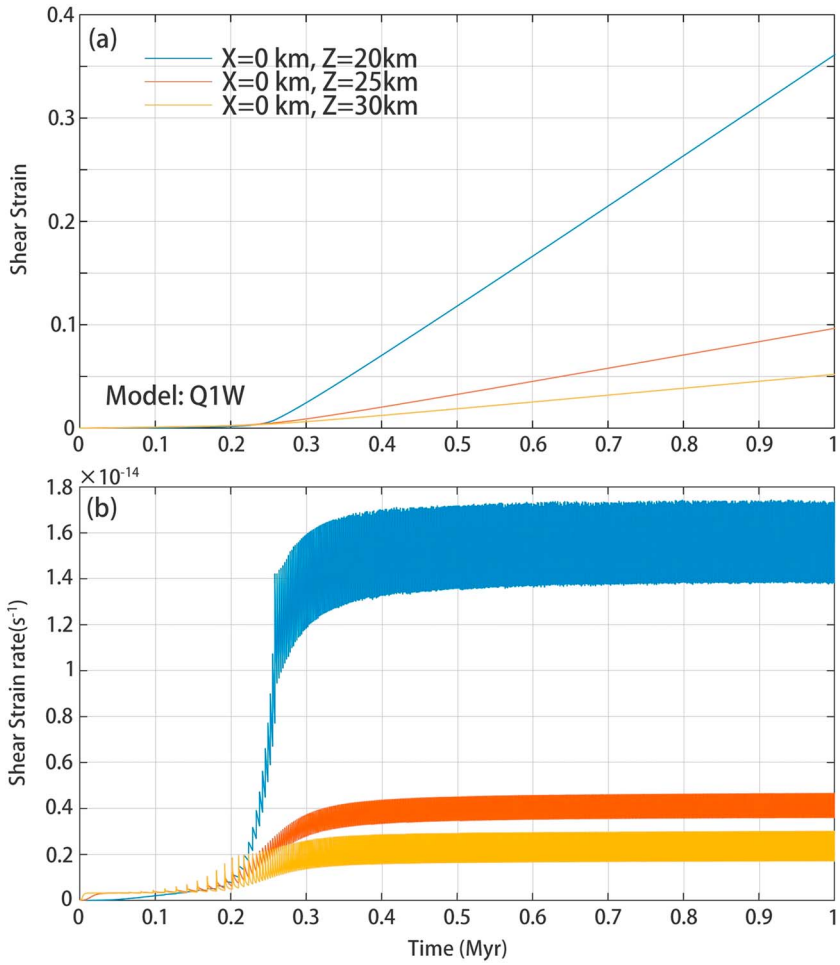

Figure 12. Shear strain (a) and shear strain rate (b) and under the fault in the lower crust. Example taken from case Q1W.

For a matured strike-slip fault whose cumulative offset is larger than several hundred meters, it is likely that shear deformation is localized in the lower crust below it and surrounding lower crust behaves in a quasi-rigid manner. Therefore, for most of known active faults, the screw dislocation model in an elastic half space (Savage & Burford, 1973) can be used to interpret the observed deformation around them and yields a reasonable estimate of the fault locking depth (Ohzono et al., 2011). The mechanical model in this study provides a physical base for the validity of the screw dislocation model. On the other hand, for strike-slip faults in their developing stages, because the deformation of the upper crust is dominated by a simple shear in the interseismic period, the similar model may not work properly.

4.3. Implication to the Discrepancy Between Geodetic and Geological Rates

For a matured fault with a large offset, such as the SAF, geodetically estimated fault slip rates are in general consistent with geological slip rates (e.g., Bourne et al., 1998). On the other hand, for many intraplate strike-slip faults, geodetically estimated slip rates are higher than geological slip rates (e.g., Meade & Hager, 2005; Ohzono et al., 2011; Oskin et al., 2008). Explanations such as the shallow slip deficit (Fialko et al., 2005), off-fault deformations (Herbert et al., 2014), and time-dependent interseismic velocity (Meade et al., 2013) may have contributed to the discrepancy between geodetic and geologic fault slip rates.

Our model calculation provides an additional clue to understand the discrepancy between geodetic and geologic fault slip rates. Figure 13a shows the calculated cumulative offsets on the fault in model Q1W together with the travel distance at the far-field boundary. The solid line in Figure 13b shows the increase rate of the cumulative offset, which is the current slip rate at the time of measurement and the gray broken line is the average fault slip rate from the beginning to the time of measurement. This result shows that even in such a simplified model, the estimated geological slip rate could be underestimated because of the delayed

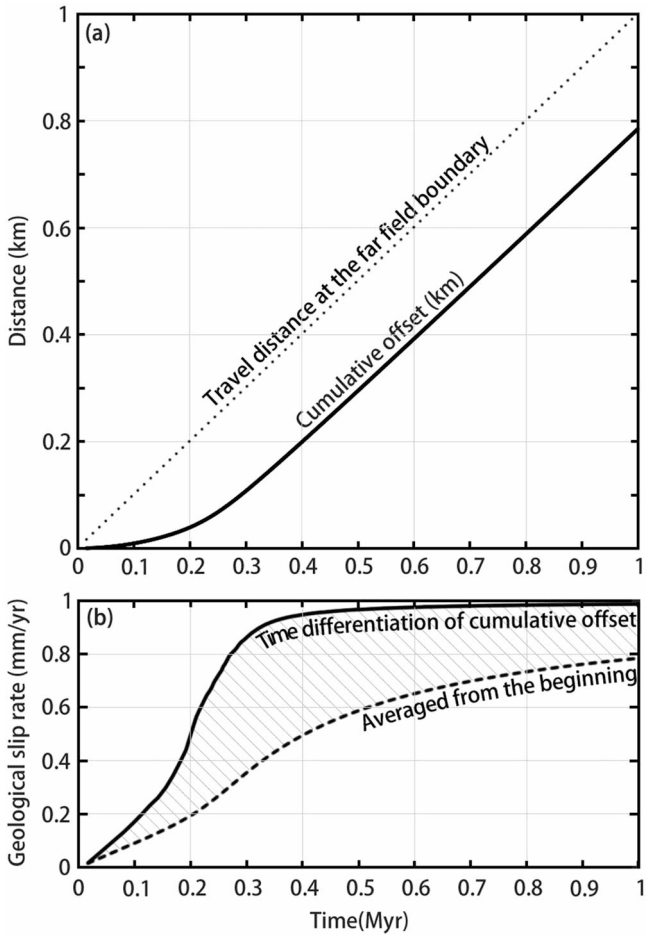

Figure 13. Cumulative fault slip (a) and geological slip rate (b) from the case of Q1W.

accumulation of the fault offset corresponding to the tectonic stress buildup. After a few millions of years of the constant tectonic loading, the geological slip rate will catch up with the geodetic slip rate.

The modeled coseismic slip is almost constant in the elastic upper crust (pink line in Figure 8b) after regular recurrence is reached and the modeled slip rate on the fault is uniform independent of the depth. However, the modeled slip rate at BDTZ is smaller than the slip rate in the shallow part because the surrounding ductile flow accommodates significant relative motion. Therefore, eroded and exposed BDTZ may represent significantly smaller relative slip rate than what would have been observed geologically.

When there is a change of the regional tectonic motion, optimally oriented faults are newly created or reactivated. But the fault offset accumulation is delayed until the tectonic stress field is created. Faults under such a condition may demonstrate a significant discrepancy between their geodetic and geologic slip rates. Such a delay effect is considered to be more common for slowly moving intraplate faults.

4.4. Comparison With Mechanical Models for Interplate Strike-Slip Fault

Previous investigations of the deformation of the lower crust and the upper mantle using mechanical models have shown that localized shear deformation can be developed in the lower crust under the interplate (e.g., Allison & Dunham, 2018; Moore & Parsons, 2015; Takeuchi & Fialko, 2012; Thatcher & England, 1998) and intraplate (e.g., Zhang & Sagiya, 2017) strike-slip faults. Some of these models considered earthquake cycles (e.g., Allison & Dunham, 2018; Erickson et al., 2017; Lambert & Barbot, 2016; Takeuchi & Fialko, 2012) and others considered a creeping fault (e.g., Moore & Parsons, 2015; Thatcher & England, 1998; Zhang & Sagiya, 2017) in the upper crust. The localized deformation in the lower crust under a fault appears in all these models. It is because the long-term behavior of the upper crust is block-like after the regular earthquake recurrence starts in all the models. Our results show that a few million years are necessary to develop a shear zone with a high shear strain (>1) in the lower crust under a slowly deforming intraplate strike-slip fault (Figure 12).

In the previous studies assuming power law rheologies for the lower crust and the upper mantle, thousands of earthquakes cycles are required for a model to reach a regular cycle (e.g., Allison & Dunham, 2018; Takeuchi & Fialko, 2012). Our simulation demonstrates that this spin-up corresponds to the tectonic stress buildup, and the fault behavior can be highly variable during this period. Without careful examination of the initial settings, unrealistic behavior appears, such as the negative shear strain rate (Takeuchi & Fialko, 2012) or extremely large shear stress right below the upper crust (e.g., Moore & Parsons, 2015; Zhang & Sagiya, 2017). Inappropriate model assumptions may have led to those unexpected results. For example, in the most of previous studies, the thickness of the upper crust is often fixed by the thickness of the seismogenic layer. This assumption is valid for those models assuming linear rheology for the lower crust (e.g., Thatcher & England, 1998). However, in the models assuming a power law rheology for the lower crust, due to the relatively low temperature in the shallow lower crust, the effective viscosity right below the upper crust becomes extremely large. In a thermomechanical model, a tremendous amount of heat is generated in the lower crust to reduce the effective viscosity (e.g., Moore & Parsons, 2015; Takeuchi & Fialko, 2012). This problem can be partially solved by calculating the depth of BDTZ for each case with different sets of rock rheology and fault strength. Through such a consideration, in Zhang and Sagiya (2017), shear stress in the lower crust is less than few hundred megapascals. On the other hand, in the uppermost part of the lower crust where effective viscosity is very high ($> 10^{24}$ Pa), only plastic deformation is allowed and the shear stress is still larger than 1 GPa. In this study, the shear stress does not exceed a few hundred megapascals (Figure 9), which is comparable to the fault strength at depth. The mechanical model in this study demonstrates that the depth of the BDTZ depends on model assumptions such as the rock rheology and boundary conditions and should not be prescribed before-

hand. Similarly, it is not appropriate to impose an elastic/brittle upper crust layer for the simulation of crustal deformation.

5. Conclusion

We have developed a self-consistent earthquake cycle model for simulating the evolution of an intraplate strike-slip fault with nonlinear Maxwell rheology. We investigate the stress buildup process in an initially stress-free crust-mantle system in the geological timescale. At the beginning of stress buildup process, the stressing rate is constant in the entire model. Due to the plastic flow, stressing rate becomes 0 in the lower crust and the upper crust. As stress increase in the upper crust, the deeper part of the upper crust with a higher strength can be broken by the earthquakes. As the fault tip is getting closer to the BDTZ, shear stress and shear strain deformation start to concentrate near the fault tip.

Before fault tip reaches the BDTZ, which depends on the fault strength, rock rheology, and total relative slip rate, the earthquakes have very long recurrence interval of ~16 kyr and in the case of 1-mm/year total relative slip rate at 50 km away from the fault. In the beginning, the recurrence interval depends on the far-field loading. The recurrence interval can also be influenced by the concentrated shear stress deformation in the lower crust as the fault tip is getting closer to the lower crust. After the regular earthquake recurrence starts, the recurrence interval decreases by an order of magnitude.

Under a slowly deforming intraplate strike-slip fault, time to develop a shear zone with large shear strain is much longer than the time for shear strain deformation to concentrates under the fault. Shear zone in the lower crust under an intraplate strike-slip fault may not be detectable with geological observations. Even without any geophysical evidence of shear zone under the intraplate strike-slip fault, simple screw dislocation model (Savage & Burford, 1973) can explain the geodetic observed deformation across the fault. Our model provides the physical explanation of the validity of the screw dislocation model.

Acknowledgments
The authors would like to thank T. Ito for providing kind supervision, helpful comments, and continued support. We thank Editor Yehuda Ben-Zion of JGR for handling the paper and one associate editor and two anonymous reviewers for their constructive reviews. This study was supported by JSPS KAKENHI Grant 26109003. The corresponding author was supported by a Japanese Government Scholarship for his study in Japan. The graphics processing unit-accelerated finite element code was developed using Partial Differential Equation Toolbox and Parallel Computing Toolbox in MATLAB. The code we developed and used in this study is available from https://github.com/Lowercrust/Viscoelastic-crust-deformation-2D.

References

Allison, K. L., & Dunham, E. M. (2018). Earthquake cycle simulations with rate-and-state friction and power-law viscoelasticity. *Tectonophysics*, *733*, 232–256. https://doi.org/10.1016/j.tecto.2017.10.021

Atwater, T. (1970). Implications of plate tectonics for the Cenozoic tectonic evolution of western North America. *GSA Bulletin*, *81*(12), 3513. https://doi.org/10.1130/0016-7606(1970)81[3513:IOPTFT]2.0.CO;2

Bourne, S., England, P., & Parsons, B. (1998). The motion of crustal blocks driven by flow of the lower lithosphere and implications for slip rates of continental strike-slip faults. *Nature*, *391*(6668), 655. https://doi.org/10.1038/35556

Bürgmann, R., & Dresen, G. (2008). Rheology of the lower crust and upper mantle: Evidence from rock mechanics, geodesy, and field observations. *Annual Review of Earth and Planetary Sciences*, *36*(1), 531.

Cowgill, E., Yin, A., Harrison, T. M., & Xiao-Feng, W. (2003). Reconstruction of the Altyn Tagh fault based on U-Pb geochronology: Role of back thrusts, mantle sutures, and heterogeneous crustal strength in forming the Tibetan Plateau. *Journal of Geophysical Research*, *108*(B7), 2346. https://doi.org/10.1029/2002JB002080

DeMets, C., & Dixon, T. H. (1999). New kinematic models for Pacific-North America motion from 3 Ma to present, I: Evidence for steady motion and biases in the NUVEL-1a model. *Geophysical Research Letters*, *26*(13), 1921–1924. https://doi.org/10.1029/1999GL900405

Elvira, P., Cornwel, D. G., & Nicholas, R. (2017). Seismic tomography of the North Anatolian Fault: New insights into structural heterogeneity along a continental strike-slip fault. *Geophysical Research Letters*, *44*, 2186–2193. https://doi.org/10.1002/2017GL072726

Erickson, B. A., Dunham, E. M., & Khosravifar, A. (2017). A finite difference method for off-fault plasticity throughout the earthquake cycle. *Journal of the Mechanics and Physics of Solids*, *109*, 50–77. https://doi.org/10.1016/j.jmps.2017.08.002

Fialko, Y., Sandwell, D., Simons, M., & Rosen, P. (2005). Three-dimensional deformation caused by the Bam, Iran, earthquake and the origin of shallow slip deficit. *Nature*, *435*(7040), 295. https://doi.org/10.1038/nature03425

Gourmelen, N., Dixon, T. H., Amelung, F., & Schmalzle, G. (2011). Acceleration and evolution of faults: An example from the Hunter Mountain-Panamint Valley fault zone, Eastern California. *Earth and Planetary Science Letters*, *301*(1), 337–344. https://doi.org/10.1016/j.epsl.2010.11.016

Henstock, T. J., Levander, A., & Hole, J. A. (1997). Deformation in the lower crust of the San Andreas Fault system in northern California. *Science*, *278*(5338), 650–653. https://doi.org/10.1126/science.278.5338.650

Herbert, J. W., Cooke, M. L., Oskin, M., & Difo, O. (2014). How much can off-fault deformation contribute to the slip rate discrepancy within the eastern California shear zone? *Geology*, *42*(1), 71–75. https://doi.org/10.1130/G34738.1

Hirth, G., & Kohlstedt, D. (2013). Rheology of the upper mantle and the mantle wedge: A view from the experimentalists. In J. Eiler (Ed.), *Inside the subduction factory*, Geophysical Monograph Series (Vol. 138, pp. 83–105). Washington, DC: American Geophysical Union. https://doi.org/10.1029/138GM06

Karato, S. (2012). *Deformation of Earth materials. An introduction to the rheology of solid Earth*. chap. 2.1.2. Cambridge: Cambridge University Press.

Kohlstedt, D. L., Evans, B., & Mackwell, S. J. (1995). Strength of the lithosphere: Constraints imposed by laboratory experiments. *Journal of Geophysical Research*, *100*(B9), 17,587–17,602. https://doi.org/10.1029/95JB01460

Lambert, V., & Barbot, S. (2016). Contribution of viscoelastic flow in earthquake cycles within the lithosphere-asthenosphere system. *Geophysical Research Letters*, *43*, 10,142–10,154. https://doi.org/10.1002/2016GL070345

Leloup, P. H., Ricard, Y., Battaglia, J., & Lacassin, R. (1999). Shear heating in continental strike-slip shear zones: Model and field examples. *Geophysical Journal International*, *136*(1), 19–40. https://doi.org/10.1046/j.1365-246X.1999.00683.x

Meade, B. J., & Hager, B. H. (2005). Block models of crustal motion in southern California constrained by GPS measurements. *Journal of Geophysical Research*, *110*, B03403. https://doi.org/10.1029/2004JB003209

Meade, B. J., Klinger, Y., & Hetland, E. A. (2013). Inference of multiple earthquake-cycle relaxation timescales from irregular geodetic sampling of interseismic deformation inference of multiple earthquake-cycle relaxation timescales from irregular geodetic sampling. *Bulletin of the Seismological Society of America*, *103*(5), 2824. https://doi.org/10.1785/0120130006

Melosh, H. J. (1976). Nonlinear stress propagation in the Earth's upper mantle. *Journal of Geophysical Research*, *81*(32).

Moore, J. D., & Parsons, B. (2015). Scaling of viscous shear zones with depth-dependent viscosity and power-law stress-strain-rate dependence. *Geophysical Journal International*, *202*(1), 242–260. https://doi.org/10.1093/gji/ggv143

Nakajima, J., & Hasegawa, A. (2007). Deep crustal structure along the Niigata-Kobe Tectonic Zone, Japan: Its origin and segmentation. *Earth, Planets and Space*, *59*(2), e5–e8. https://doi.org/10.1186/BF03352677

Nakajima, J., Kato, A., Iwasaki, T., Ohmi, S., Okada, T., & Takeda, T. (2010). Deep crustal structure around the Atotsugawa fault system, central Japan: A weak zone below the seismogenic zone and its role in earthquake generation. *Earth, Planets and Space*, *62*(7), 555–566. https://doi.org/10.5047/eps.2010.06.007

Ogawa, Y., & Honkura, Y. (2004). Mid-crustal electrical conductors and their correlations to seismicity and deformation at Itoigawa-Shizuoka Tectonic Line, Central Japan, Earth. *Planets and Space*, *56*(12), 1285–1291. https://doi.org/10.1186/BF03353352

Ohzono, M., Sagiya, T., Hirahara, K., Hashimoto, M., Takeuchi, A., Hoso, Y., et al. (2011). Strain accumulation process around the Atotsugawa fault system in the Niigata-Kobe Tectonic Zone, central Japan. *Geophysical Journal International*, *184*(3), 977–990.

Oskin, M., Perg, L., Shelef, E., Strane, M., Gurney, E., Singer, B., & Zhang, X. (2008). Elevated shear zone loading rate during an earthquake cluster in eastern California. *Geology*, *36*(6), 507. https://doi.org/10.1130/G24814A.1

Rutter, E., & Brodie, K. (2004). Experimental intracrystalline plastic flow in hot-pressed synthetic quartzite prepared from Brazilian quartz crystals. *Journal of Structural Geology*, *26*(2), 259–270. https://doi.org/10.1016/S0191-8141(03)00096-8

Rybacki, E., Gottschalk, M., Wirth, R., & Dresen, G. (2006). Influence of water fugacity and activation volume on the flow properties of fine-grained anorthite aggregates. *Journal of Geophysical Research*, *111*, B03203. https://doi.org/10.1029/2005JB003663

Savage, J. C., & Burford, R. O. (1973). Geodetic determination of relative plate motion in central California. *Journal of Geophysical Research*, *78*(5), 832–845. https://doi.org/10.1029/JB078i005p00832

Savage, J. C., & Prescott, W. H. (1978). Asthenosphere readjustment and the earthquake cycle. *Journal of Geophysical Research*, *83*(B7), 3369–3376. https://doi.org/10.1029/JB083iB07p03369

Savage, J. C., Svarc, J. L., & Prescott, W. H. (1999). Geodetic estimates of fault slip rates in the San Francisco Bay area. *Journal of Geophysical Research*, *104*(B3), 4995–5002. https://doi.org/10.1029/1998JB900108

Sclater, J. G., Jaupart, C., & Galson, D. (1980). The heat flow through oceanic and continental crust and the heat loss of the Earth. *Reviews of Geophysics*, *18*(1), 269–311. https://doi.org/10.1029/RG018i001p00269

Sibson, R. H. (1982). Fault zone models, heat flow, and the depth distribution of earthquakes in the continental crust of the United States. *Bulletin of the Seismological Society of America*, *72*(1), 151–163.

Stern, T., Okaya, D., Kleffmann, S., Scherwath, M., Henrys, S., & Davey, F. (2007). Geophysical exploration and dynamics of the Alpine fault-zone. In D. Okaya, T. Stern, & F. Davey (Eds.), *A Continental Plate Boundary: Tectonics at South Island, New Zealand* (Vol. 175, pp. 207–233). Washington, DC: American Geophysical Union.

Stirling, M. W., Wesnousky, S. G., & Shimazaki, K. (1996). Fault trace complexity, cumulative slip, and the shape of the magnitude-frequency distribution for strike-slip faults: A global survey. *Geophysical Journal International*, *124*(3), 833–868. https://doi.org/10.1111/j.1365-246X.1996.tb05641.x

Takeuchi, C. S., & Fialko, Y. (2012). Dynamic models of interseismic deformation and stress transfer from plate motion to continental transform faults. *Journal of Geophysical Research*, *117*(B5), B05403. https://doi.org/10.1029/2011JB009056

Thatcher, W., & England, P. C. (1998). Ductile shear zones beneath strike-slip faults: Implications for the thermomechanics of the San Andreas Fault zone. *Journal of Geophysical Research*, *103*(B1), 891–905. https://doi.org/10.1029/97JB02274

Weber, M., Abu-Ayyash, K., Abueladas, A., Agnon, A., Al-Amoush, H., Babeyko, A., et al. (2004). The crustal structure of the dead sea transform. *Geophysical Journal International*, *156*(3), 655–681. https://doi.org/10.1111/j.1365-246X.2004.02143.x

Wilson, C. K., Jones, C. H., Molnar, P., Sheehan, A. F., & Boyd, O. S. (2004). Distributed deformation in the lower crust and upper mantle beneath a continental strike-slip fault zone: Marlborough fault system, South Island, New Zealand. *Geology*, *32*(10), 837. https://doi.org/10.1130/G20657.1

Wittlinger, G., Masson, F., Poupinet, G., Tapponnier, P., Mei, J., Herquel, G., et al. (1996). Seismic tomography of northern Tibet and Kunlun: Evidence for crustal blocks and mantle velocity contrasts. *Earth and Planetary Science Letters*, *139*(1), 263–279. https://doi.org/10.1016/0012-821X(95)00235-5

Wittlinger, G., Tapponnier, P., Poupinet, G., Mei, J., Danian, S., Herquel, G., & Masson, F. (1998). Tomographic evidence for localized lithospheric shear along the Altyn Tagh fault. *Science*, *282*(5386), 74–76. https://doi.org/10.1126/science.282.5386.74

Yoshimura, R., Oshiman, N., Uyeshima, M., Toh, H., Uto, T., Kanezaki, H., et al. (2009). Magnetotelluric transect across the Niigata-Kobe Tectonic Zone, central Japan: A clear correlation between strain accumulation and resistivity structure. *Geophysical Research Letters*, *36*, l20311. https://doi.org/10.1029/2009GL040016

Zhang, X., & Sagiya, T. (2017). Shear strain concentration mechanism in the lower crust below an intraplate strike-slip fault based on rheological laws of rocks. *Earth, Planets and Space*, *69*(1), 82. https://doi.org/10.1186/s40623-017-0668-5

Zhu, L. (2000). Crustal structure across the San Andreas Fault, southern California from teleseismic converted waves. *Earth and Planetary Science Letters*, *179*(1), 183–190. https://doi.org/10.1016/S0012-821X(00)00101-1